


RESEARCH

Open Access



A modified model for laser-cornea interaction following the ablation effect in the laser eye-surgery

Ibrahim Abdelhalim¹, Omnia Hamdy^{1*} , Aziza Ahmed Hassan², Salwa Abdelkawi³ and Salah Hassab Elnaby¹

Abstract

Background Laser corneal reshaping is a successful treatment of many refraction disorders. However, some physical demonstrations for the laser interaction with cornea are not fully explained. In the current paper, we present a modified model to precisely investigate the ablation threshold, the ablation rate and the physical/chemical mechanisms in that action.

Results The model discusses the possible photochemical reaction between the incident photons and various components of the cornea. Such photochemical reaction may end by photo-ablation or just molecular electronic excitation. The ablation threshold is also produced by other chemical reaction. Finally another chemical reaction creates out-site fragments. Moreover, the effect of applying different laser wavelengths, namely the common excimer-laser (193-nm), and the solid-state lasers (213-nm & 266-nm) has been investigated.

Conclusion Despite the success and ubiquity of the Argon Fluoride “ArF” laser, our results reveal that a carefully designed 213-nm laser gives the same outcomes with the potential of possible lower operational drawbacks related with heat generation and diffusion.

Keywords Mathematical modeling, Laser ablation, Cornea, Photochemical reaction

1 Background

Recently, scientists have focused their attention on comprehending the intricate dynamics of numerous physiological behaviors in different medical conditions and treatment procedures [1, 2]. By modeling it and attempting to discover approximate solutions, mathematics played a significant role in understanding the mechanism of the transmission of various infectious diseases (e.g.

COVID-19) [3] and cancer [4]. Lasers have been utilized in corneal reshaping for refractive correction since several decades [5–7]. The practice of the procedure has been much advanced than the theoretical explanation. Due to the presence of many chemical and physical processes, an exact set of equation governing the procedure seemed out of reach or out of interest. The presence of several tissues with slightly and/or significantly different parameters, and individual differences complicates reaching an exact simulation. Different authors developed models adapted to certain experimental results on phantom, ex vivo and in vivo subjects. However, in most of the mathematical models of biological systems, finding appropriate parameter values presents a problem [8]. Additionally, phytochemical analysis has shown great importance in multiple techniques for the study of treatments and image cases in different scientific problems related to medicine [9, 10].

*Correspondence:

Omnia Hamdy
omnia@niles.cu.edu.eg

¹ Engineering Applications of Laser Department, The National Institute of Laser Enhanced Sciences, Cairo University, Giza 12613, Egypt

² Medical Applications of Laser Department, The National Institute of Laser Enhanced Sciences, Cairo University, Giza 12613, Egypt

³ Vision Science Department, Research Institute of Ophthalmology, Biophysics and Laser Science Unit, Giza, Egypt

Models of heat transport in the eye have previously been presented in the literature. Taflove et. al. [11] assumed that the eye is homogeneous and used a finite difference model to study the temperature distribution due to absorption of microwave. While Al-Badwaih et. al. [12] presented a simple heat transport model to examine the thermal effects of microwave radiation on the human eye. They used simplified eye structure to permit a steady-state analytical solution which cannot be extended to simulate time varying solution. Moreover, applying the finite element method of solution on the rabbit eye was employed in [13]. The iris and ciliary body were included as part of the boundary of the domain. The model was used to calculate the initial temperature distribution in the normal unexposed rabbit eye and the temperature rises induced by exposure to microwave radiation. In 1982, Lagendijk [14] developed model that used a simple explicit forward-difference heat balance technique. Both transient and steady-state calculations were performed.

When material is removed from a solid (or occasionally liquid) surface by being exposed to a laser beam, the process is known as laser ablation or photoablation. Low laser flux causes the substance to heat up and evaporate or sublime as a result of the absorbed laser energy. The substance usually turns into plasma at high laser flux levels. Additionally, the covalent bonds in the polymer chains are broken by the energy of the UV photons, which causes photochemical ablation [15]. Corneal ablation using ultraviolet (UV) short pulsed lasers doesn't rise the temperature of the eye to significant values [16]. The later feature makes the UV-laser wavelengths with nano-second or shorter pulse duration more suitable for ablation. Therefore, models for polymeric materials and for corneal tissue have been developed. Pettit et. al [17] developed a model that included the effects of chromophore saturation and multiphoton absorption. While, Fisher et. al. [18] excluded experimentally the formation of plasma during the photoablation process by direct fluorescence measurement. Tokarev et. al. [19] presented a model based on the thermal effect that evaporates tissues and its resulting chemical decomposition. The evaporation may not be a basic step for the chemical decomposition. However any model should consider the heat generated in the chemical process; this heat is not sufficient for the molecular decomposition.

Sutcliffe et. al. [20] proposed a model based on the ablative photodecomposition, in which a critical density of broken bonds results from an incident photon flux above a certain threshold density (i.e., ablation threshold). The novel concepts of the ablation threshold and the ablative absorption coefficient that is larger than the preablative (i.e., static) value have been deeply illustrated in [21].

However, the transient changes in absorption coefficient within layers of material caused by the photo decomposition of long-chain molecules and chromophores prior to reaching the ablation threshold were neglected. However, the best-fit parameters for 193-nm ablation led to unrealistic values, which the authors concluded to be indicative of a significant change in ablation mechanism at the short ArF laser wavelength.

Many aspects of the primary processes and secondary effects of UV corneal photoablation are still not completely understood.

At first look, the success of Photorefractive keratectomy (PRK) and Laser-assisted in situ keratomileusis (LASIK) indicates that the missing information is not a critical issue with current delivery systems that aim at correcting mainly spherical refraction with an accuracy of approximately ± 0.50 diopters. Current state-of-the-art systems attempt to correct both spherical equivalent and astigmatism with significant attempts to correct higher order aberrations. Typically, ultrasonography, Pentacam, and noncontact devices such as the Visante anterior segment optical coherence tomographer (ASoptical coherence tomography (OCT)) are becoming more common to evaluate ocular parameters [22]. However, a better understanding of the ablation process could improve the precision of higher aberration correction. Additionally, exploring of the healing process is likely also needed for best results.

The current work consequently proposes a modified model that offers new insights regarding the ablation threshold, the ablation rate, and the physical and chemical mechanisms underlying that action. The model shows the potential photochemical and chemical interactions between incident photons and different corneal components after using various UV lasers, such as the conventional ArF excimer (193 nm) and substitute solid-state lasers at 213 and 266 nm. We here present a model to try to accommodate many results in our lab and some other published results.

2 Model description

2.1 constructing the eye model

The human eye is usually approximated geometrically as a set of arcs with different radii, rotated around the axis of symmetry (optical axis). This axis is defined by the center of the eye and the lens [23]. The geometry of the eye structure utilized in this model and all the mathematical computations were created under the environment of MATLAB R2022b platform. The cornea represents more than 65% of the focusing power of the eye; consequently, any alteration in the cornea's curvature leads to significant eye refraction error. Moreover, individual differences in corneal characteristics, such as thickness,

composition, and hydration, can undoubtedly affect how the cornea reacts to laser irradiation. However, it is difficult to include these inter-individual variances in a mathematical model. As a result, the suggested model is independent of biological variability. However, the experimental research must take this aspect into account.

A preliminary simulation of laser heating of the eye is performed with laser pulse energy 1 J and pulse duration 5 ns. This simulation revealed that the temperature of parts of eye beyond a radial distance of 5 mm still have the initial temperature (Figure 1(a)).

Accordingly, in our proposed model, to increase the mesh accuracy and while keeping reasonable processing time, we concentrated on a part of cornea inside a cylinder of radius 3 mm coaxial with the laser axis and height 1400 μm as presented in Figure 1(b). The increment in r and z coordinates $dr=dz=0.8 \mu\text{m}$. The increment in time dt for the photochemical reaction is 6.6×10^{-17} sec. The region investigated $r = -3:3 \text{ mm}$ $z=0 - 1.4 \text{ mm}$. The volume is 39.58 mm^3 . Volume of one cell = $0.512 \mu\text{m}^3$.

2.2 The physical parameters

The physical parameters of normal human cornea are summarized in Table 1 [24, 25].

Our developed algorithm have been verified with the thermal effect of corneal tissue produced using some commercial laser ophthalmic devices for eye microsurgery including Zeiss Mel 90, Pulzar Z1, Katana laser soft and Medilex. Table 2 illustrates the main technical specifications for the equipment assuming the initial temperature of the cornea is 26.9°C [16]. The values of the parameters in Table 2 correspond to the operational

Table 1 The physical parameters of human cornea

Rate of blood perfusion (1/s)	Metabolic flux (W/m ³)	Thermal conductivity (w/m °C)	Specific heat (J/Kg °C)	Density (kg/m ³)
0	0	0.580	4178	1050

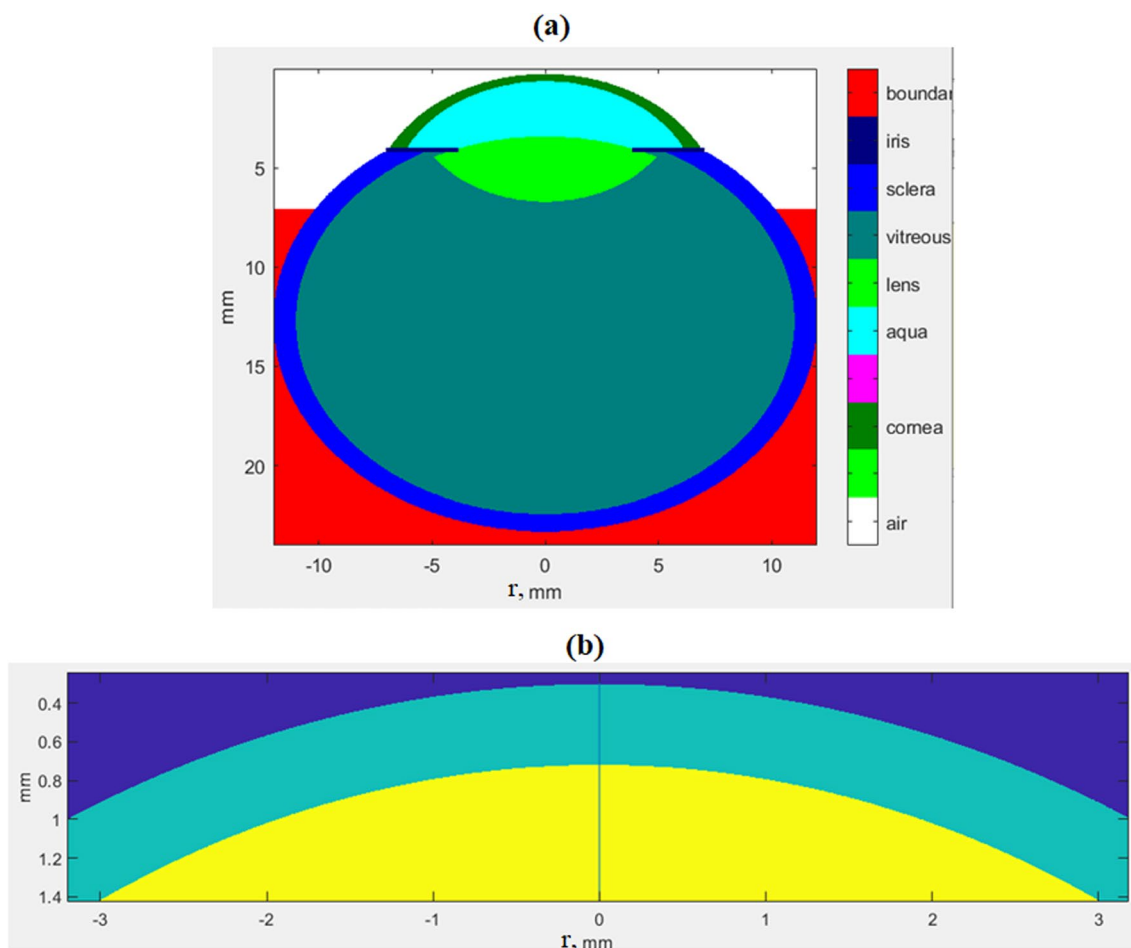


Fig. 1 The implemented eye-model **a** the whole structure of the eye, **b** the cornea

Table 2 Technical specifications of common laser eye-surgery devices [27]

Device	Wavelength (nm)	Active medium	Pulse duration (ns)	Beam type	Energy (mJ)	Spot size (mm)	Absorption coefficient (m ⁻¹)
Medilex	222	KrCl	15	Broad beam	250	0.2–5	208,366
	248	KrF	15	Gaussian	250	0.2–0.5	48,277
Zeiss Mel 90	193	Arf	4–7	Flying Spot Gaussian	1	0.7	270,000
Pulzar Z1	213	Nd:YAG fifth harmonic	10–12	Flying Spot Gaussian	1	0.6	230,300
katana laser soft	210	Ti_sapphire fourth harmonic	> 5	Flying Spot Near Gaussian	< 0.1	0.2	232,000

parameters of the current commercial systems. The UV absorption coefficient was measured in the UVA region by Kolozsva et al [26].

Because the refraction index of the cornea in the far UV region is unknown, the reflection loss contribution to the measured absorbance cannot be calculated accurately. However, it is estimated from the refraction index of water so reflection is estimated smaller than 0.1 in this spectral region. The linear absorption coefficient “a” has been determined to be $2300 \pm 330 \text{ cm}^{-1}$ at 210 nm and $2410 \pm 370 \text{ cm}^{-1}$ at 193 nm from 23 samples of 18 porcine corneas. Similar results for human corneas are $2320 \pm 470 \text{ cm}^{-1}$ at 210-nm and $2340 \pm 450 \text{ cm}^{-1}$ at 193 nm from 11 samples of six human corneas [26]. It can be mentioned here that the absorption cross section are usually determined by applying Beer’s law via measuring the incident intensity and transmitted intensity after passing a defined thickness. The losses of intensity in the UV spectrum are due to thermal absorption (energy converted to heat), multiple internal scattering and photochemical reactions. The last one is significant in this region of wavelengths. That is why when using the heat equation we should use only the value of thermal absorption cross section (i.e. thermal absorption coefficient of corneal tissue).

Reduced thermal absorption means that the cornea absorbs less heat from the laser energy. Consequently, when the cornea has low thermal absorption properties, it requires less laser energy to achieve the desired ablation depth. This means that each laser pulse removes more corneal tissue, resulting in a higher rate of change of ablation per pulse. In contrast, when the cornea has high thermal absorption properties, it absorbs more heat from the laser energy, requiring more laser pulses to achieve the same ablation depth. This leads to a lower rate of change of ablation per pulse [28]. In our model we consider the thermal absorption cross section as one of the parameters to be determined. So this value is expected to be smaller than the published absorption cross section.

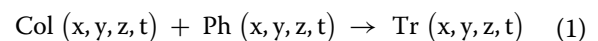
Fundamentally, laser pulses can have a very wide range of fluxes and durations (from milliseconds to femtoseconds) with the ability to be precisely controlled. However, in high frequency pulses there will be accumulation of fragments and also temperature rises, which may affect the consequential ablation rate [29]. In this model we didn’t consider these effects as we focused on the chemical reactions.

2.3 Reactions

The proposed model is slightly different from Fisher’s model [18], we considered one photochemical reaction and two chemical reactions.

2.3.1 The photochemical reaction

The ablation may occur as a two-step reactions as described by Fisher et. al. [18]. The photochemical reaction converts collagen molecules to some transient products.



where Col represents the collagen molecular density, Ph represents the photon number density and Tr represents the density of transient products. Then these transient molecules will undergo a chemical reaction with water to produce final fragmented molecules that is dispersed away. The rate of the 1st reaction is given by a linear reaction coefficient as follows:

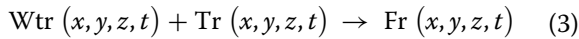
$$\frac{\partial y}{\partial x} \text{Tr}(x, y, z, t) = -K_1 \cdot \text{Col}(x, y, z, t) \cdot \text{Ph}(x, y, z, t) \quad (2)$$

where, K_1 is the photochemical reaction constant [m^3s^{-1}].

2.3.2 The chemical reactions

The chemical reaction is classified to two reactions. The 1st chemical reaction produces molecular fragments. While the second chemical reaction is a reverse reaction in the opposite direction intended to explain the observed ablation threshold.

2.3.2.1 The forward reaction The first chemical reaction (the forward reaction) is defined as:



where W_{tr} is the number density of water molecules, F is the number density of final fragmented products. Some species of the products may accumulate in the hole produced by ablation, while others leave the place. These accumulated molecules could be CO_2 molecules that can absorb incident photons and thus reduce the rate of ablation as the number of pulses increase. This may explain the observed reduction of ablation rate for higher number of pulses. This effect was not considered here. The rate of the 2nd reaction (the chemical reaction that produces the ablation products “forward reaction”) is also linear [m^3s^{-1}]:

$$\frac{\partial y}{\partial x} Fr(x, y, z, t) = K_2 Tr(x, y, z, t) \cdot W_{tr}(x, y, z, t) \quad (4)$$

where, K_2 is the rate of the reaction. The absorption coefficient α [m^{-1}] is defined as:

$$a = s_{air} \times r_{air} + s_{cor} \times r_{cor} + s_{Tr} \times r_{Tr} + s_{Fl} \times r_{Fl} + s_{W_{tr}} \times r_{W_{tr}} \quad (5)$$

where, α_{air} , α_{cor} , α_{Tr} , α_{Fl} and $\alpha_{W_{tr}}$ are the molecular absorption cross sections [m^2] and ρ_{air} , ρ_{cor} , ρ_{Tr} , ρ_{Fl} and $\rho_{W_{tr}}$ are the concentration in [m^{-3}] of air, corneal tissue, transients, final products and water respectively.

2.3.2.2 Backward reaction It was necessary to assume another reaction that may take place. This reaction is the second chemical reaction introduced in 2.3.2. Such reaction is common in many similar situations, where molecules that have just been broken to two smaller molecules by bond breaking, may recombine again. This recombination is a function of the transient molecules, and independent on the photon density. So for low photon density the transient molecules that will continue to react with water to produce final fragments would be very little or null. However for higher photon density the production of transient molecules can overcome recombination and so ablation can be observed. The rate of recombination reaction can be determined by fitting experimental results. This recombination reaction strongly explains the observed ablation threshold.

$$\frac{\partial}{\partial t} Fr(x, y, z, t) = K_r (Tr(x, y, z, t))^2 \quad (6)$$

where, K_r is the rate of the (backward) reverse reaction. Since this reaction is a doubly chemical reaction that recombines two molecules of the transient products, the rate depends on the square of the molecular density.

2.4 Temperature rise

There are two types of energy absorbed by the tissues and result in temperature rise. The first is the photons that do not break the bond. The second source comes from the difference between the bond energy and the photon energy. The model shows that not all the incident photons energy is used to break the bond. So the rest of photon energy is absorbed as heat. This difference in energy is absorbed by the transient molecules using their high absorption coefficient. The heat diffusion equation is used to estimate the temperature rise in eye tissues. This is an added source of heating, previous models didn't consider this effect. So a key contribution of this model is considering this source of energy.

Due to the inhomogeneity and the presence of different species the physical parameters can vary from one point to another. So the heat equation for the considered region can be expressed in cylindrical coordinates as:

$$\rho c_p \frac{\partial T}{\partial t} = \frac{1}{r} \frac{\partial}{\partial r} \left(kr \frac{\partial T}{\partial r} \right) + \frac{1}{r^2} \frac{\partial}{\partial \phi} \left(kr \frac{\partial T}{\partial \phi} \right) + \frac{\partial}{\partial z} \left(\frac{\partial T}{\partial z} \right) + q_v \quad (7)$$

where k is the material thermal conductivity [$Wm^{-1} K^{-1}$], ρ is material density [m^3], c_p is the material specific heat at constant pressure [$J Kg K^{-1}$], q_v is the rate of energy generated due to photon absorption per unit volume [Wm^{-3}] and T is the absolute temperature as function of z , r and t . The laser intensity is I defined by:

$$I(z, r, t) = \frac{F}{\sqrt{2\pi}S} \exp\left(-\frac{t^2}{2S^2}\right) \exp\left(-\frac{r^2}{2w^2}\right) \exp(-\alpha \cdot z) \quad (8)$$

where F is laser fluence [Jm^{-2}], S is the standard deviation of the time pulse profile (assumed to be Gaussian) and w is the radius of the Gaussian beam [m]. α is the total extinction coefficient [m^{-1}].

The boundary condition is assumed to be radiative and convective on the surface of the cornea and constant T_o at the bottom. While for the upper surface of the cornea, the rate is:

$$k \frac{\partial T}{\partial n} = \sigma_B \epsilon (T - T_a) + h(T - T_o) \quad (9)$$

where n is the normal to the boundary layer, h is the convective heat transfer coefficient between corneal surface and air ($10W/m^2 K$), σ_B Boltzmann constant ($5.67 \times 10^{-8} Wm^{-2} K^{-4}$), ϵ is the emissivity of the corneal surface (0.975), T_o is the initial temperature of the eye assumed to be $27^\circ C$ (300 K) and T_a is the ambient temperature assumed to be $25^\circ C$ (298 K). In clinical practices, T_o at the bottom of the cornea may be

non-constant. However, in our model we study the ablation effect mainly on the corneal surface. Accordingly, T_o was assumed to be constant.

2.5 Experimental verification

Previously published data for corneal ablation using 193 nm, 213 nm and 266 nm have been used in verification of the proposed model [18]. Additionally, results for PMMA ablation by 266 nm solid state laser were utilized. The details of the experimental setup and results can be found elsewhere [30].

The photochemical reaction takes place in extremely short time. Fisher et. al. [18] estimated the photochemical reaction rate to be $k_1 = 7.1 \times 10^{-10} \text{ cm}^3\text{s}^{-1}$, and a chemical reaction rate $k_2 = 3.7 \times 10^{-17} \text{ cm}^3\text{s}^{-1}$. They assumed a one photon reaction with collagen to produce intermediate products and one chemical reaction between water and these products to produce final debris that is removed from the cornea. They used an estimation of the number of peptide molecules to be $1.354 \times 10^{21} \text{ cm}^{-3}$; also they used absorption cross section of peptide at 193 nm as $1.19 \times 10^{-17} \text{ cm}^2$ and that of transient components $4.5 \times 10^{-15} \text{ cm}^2$ and the absorption cross section of end products to be $4.5 \times 10^{-24} \text{ cm}^2$. From here onward we are going to use the standard metric system MKS of units. So we consider the peptide density to be $2.0256 \times 10^{27} \text{ m}^{-3}$.

First, we considered the absorption cross section of peptide to be $1.19 \times 10^{-21} \text{ m}^2$ and that of transient $4.5 \times 10^{-19} \text{ m}^2$. This leads to absorption coefficient $2.4097 \times 10^6 \text{ m}^{-1}$. Then after establishing the relation of the ablation rate w.r.t absorption coefficient we showed the value of the absorption cross section that gives the best fit to the experimental data.

The assumptions in [18] are quite simple and straightforward. We have tried to use these findings to fit the results of photo ablation of cornea by 266 nm laser to achieve results that are close to the experimental results.

The ablation rate (ablation depth per pulse) increases at the beginning and then stabilizes with tendency to very little decrease. The startup increase can be attributed to the accumulation of transient species which is converted to fragmented species. After some pulses another accumulation of fragment species reduces the light intensity absorbed by corneal tissues as shown in Fig. 2. This tendency agrees with the experimental results [30].

Our model considers the case of pulse train incident on a single spot. We do not believe that the currently systems using flying spot may have nearly similar ablation rates, although they should have lower temperature rise. Still our model is correct as a comparison between different systems. Ablation rate is affected by three main parameters, we have to estimate these parameters by fitting our model to the published results, and then

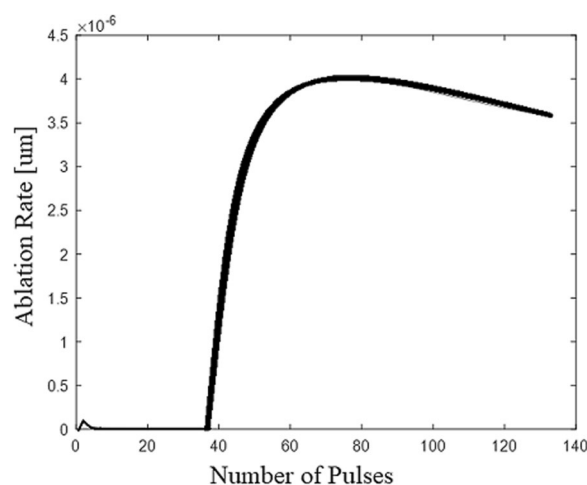


Fig. 2 Behaviour of Ablation rate with number of laser pulses

we compare our experimental results using 266 nm to the proposed model. These parameters have a combined effect on the resulting ablation.

2.5.1 Thermal absorption

There are several estimated values of the absorption cross section of corneal tissues. However the decomposed molecules are not very well identified and little is known about its absorption cross section. To understand the effect of the absorption cross section of transient products we used three different values $\alpha_1 > \alpha_2 > \alpha_3$. Figure 3 shows the rate of change of ablation per pulse increases with decreasing the thermal absorption (keeping other parameters constant) this is shown by the curves $G_{1,1}$, $G_{1,2}$ and $G_{1,3}$ respectively.

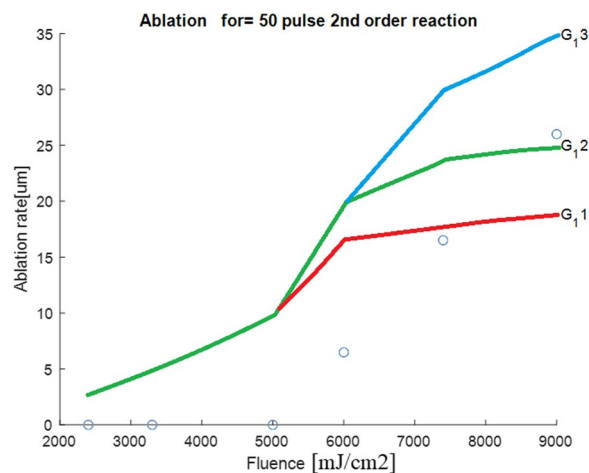


Fig. 3 Ablation rate vs. Fluence for different absorption cross section

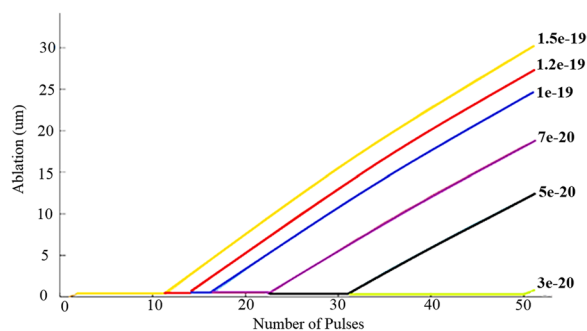


Fig. 4 Ablation rate for different values of (K_1) at the same fluence

2.5.2 Photochemical reaction K_1

The photochemical rate of reaction is a very important parameter. To understand its effect we examined many values of K_1 . Figure 4 shows the relation between ablation rate and number of pulses near the threshold condition for different values of K_1 .

2.5.3 The chemical reaction K_2

The chemical rate of the second reaction which produces the final products is another important parameter. We started by the published values and improve them gradually to fit the published results.

2.5.4 The chemical reverse reaction K_r

We assumed that this parameter have a role in defining a threshold for the ablation process. It also varies in the case of laser at 266 nm than that of 193 nm since the decomposed molecules could be different.

The implementation steps of our proposed model can be summarized as follows:

1. We find an ensemble of absorption coefficients that produces ablation curve with the nearest slope to the experimental results.
2. Using the absorption coefficients obtained in the previous step, we find triplets (K_1 , K_r and absorption coefficients) that mimic the threshold and the maximum value of ablation.
3. The least square function of the selected triplets has been optimized to get the model with minimum least square deviation from the experimental published results.
4. We tried to keep K_r and K_2 the same values for both 193 nm and 266 nm. This assumption that the decomposed molecules could be the same can't rule out the possibility of having different molecules when using different wavelengths. This assumption can only be verified through time resolved Raman spectroscopy.

5. We constructed a 3-valued function (f) that maps any set of combinations of K_1 , K_r and α to a value representing the least square error of the calculated ablation rate using this set and the actual measured values. The optimum set should satisfy the following conditions:
6. Obtaining minimum least square error
7. Satisfying the threshold value
8. No ablation can be measured for fluence less than the threshold value.

2.6 Minimum value of the function $f(K_1, K_r, \alpha)$

Assuming that $f(K_1, K_r, \alpha)$ is continuous and differentiable then the necessary condition for the minimum point (actually it is local minimum) is that the gradient of the function vanishes at every local minimum $\nabla f(K_{1m}, K_{rm}, s_m) = 0$. That is all partial derivatives vanish at that point. We get several local minimums then we choose the absolute minimum of the function.

2.7 Effect of the spatial and temporal steps

The spatial step dz and temporal step dt was found to satisfy the stability and convergence of the solution. In the same time we tried to minimize the computational time as much as we can. Here are some values. All of them satisfy the stability condition we fixed the error due to conversion to about 1% or less. Spatial increment in r and z coordinates $dr = dz = 0.8$ nm. The increment in time dt for the photochemical reaction is 6.6×10^{-17} s. These are the optimum choice in view of the reaction rates. Table 3 shows the effect of temporal and spatial increments for 5 s of 10 Hz laser and pulse duration $Taw = 5$ ns, and Gaussian beam of diameter 1.3 mm.

3 Results

3.1 Parameters for 193-nm ablation

The obtained results have been presented as a group of sub-plots for each case. For example for the case of 213 nm laser ablation (Fig. 5) with fluence 250 mJ/cm², and using the following parameters $K_1 = 0.6 \cdot 10^{-19}$ m³s⁻¹, $K_r = 10^{-19}$ m³s⁻¹ and $K_2 = 3.7e^{-23}$ m³s⁻¹. The subplot (A) shows the temperature profile after 50 pulses along the laser axis. The portion of absorption coefficient due to photo-chemical reaction is in heading of subplot (B) in m⁻¹. The relative concentration of peptide molecules along the laser axis after 50 pulses is shown in subplot (C). While the variation in the thermal absorption coefficient with time is presented in subplot (D). Subplots (E), (F), (G) and (H) show the spatial distribution of temperature, peptide molecules density, transient products density and fragment density respectively. Transients' life time is too short so it didn't appear in the plot.

Table 3 The effect of the temporal and spatial increments on the resultant parameters

dz [um]	dt	Temp.[K]	Fragments density [Kgm ⁻³]	Ablation depth [um]	Calculation time
0.001	Taw/9.9×10 ⁵				5087 h
0.01	Taw/10				5.5 h
0.01	Taw/100				
0.01	Taw/1000				
0.1	Taw/10	325.9	1.06 10 ²⁷	34.5	10 min
0.1	Taw/100	326.2	1.06 10 ²⁷	34.1	
0.1	Taw/1000	325.3	1.06 10 ²⁷	34.1	

The deviation between the ablation results is not significant. We choose dz=0.1um and dt=Taw/100 as compromise between execution speed and precision

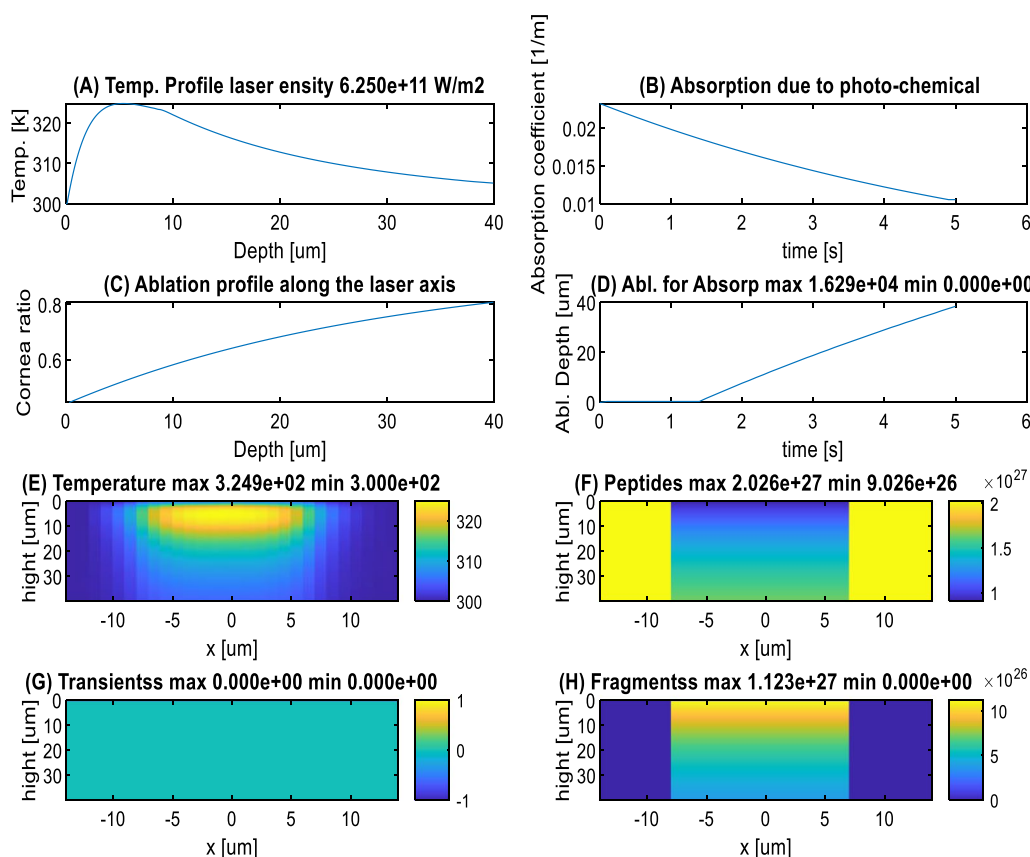


Fig. 5 Results of laser ablation using 193 nm, **A** the temperature profile after 50 pulses along the laser axis, **B** The portion of absorption due to photo-chemical reaction, **C** the ablation profile along the laser axis, **D** the variation in the thermal absorption coefficient with time, **E** the spatial distribution of temperature, **F** peptide molecules density, **G** transient products density, **H** fragment density

When applying the model to experiments using ArF laser we used the ablation rate data given by Munnerlyn et. al [31]. Several triplet parameters have been studied; we present here some samples as in Table 4. We postulated that a reverse reaction takes place on the transient products and recombine them to peptides. The effect of the reverse reaction doesn't depend on the laser fluence but depends on the transient compounds densities. We

Table 4 Parameters for 193 nm

	$K_1 \times 10^{-20}$ m^3s^{-1}	$K_r \times 10^{-19}$ m^3s^{-1}	Thermal absorption [m ⁻¹]	Least square error $\times 10^{-4}$
F40	8	1	24,307	1.87
F41	15	1	24,307	0.143
F31	6	1	15,800	2.815
F34	5.5	1	17,015	2.665

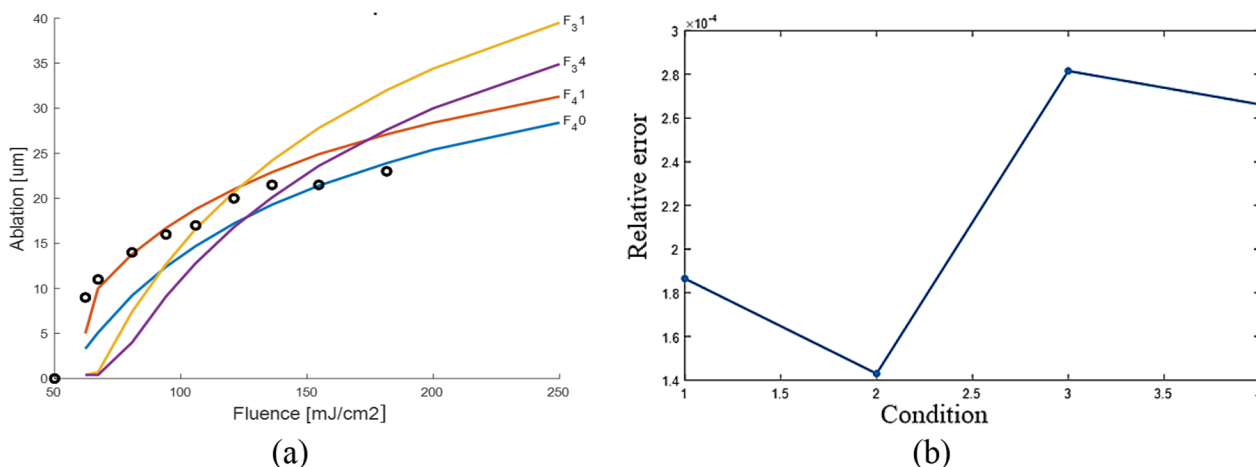


Fig. 6 a Ablation versus fluence after 50 pulses laser at 193 nm, b The least square error

Table 5 Parameters for 213 nm

	$K_1 \times 10^{-20}$ m^3s^{-1}	$K_r \times 10^{-19}$ m^3s^{-1}	Thermal absorption $[m^{-1}]$	Least square error $\times 10^{-4}$
F40	8	1	24,307	3.423
F41	10	1	24,307	2.824
F31	6	1	17,015	1.25
F34	5.5	1	15,800	1.761

start by choosing the K_r to give the observed threshold, then using the least square to find the best fit. Plotting the slope of the curve with respect to coefficient of absorption shows clearly the inverse relation between them, i.e. the high absorption results in slow ablation and vice versa. The plot of ablation rate versus the fluence is presented in Fig. 6. Additionally, Table 5 illustrates some of the combinations between ablation rate and the fluence.

The optimum triplet was reverse reaction chemical rate $1 \times 10^{-19} m^3/s$, photochemical reaction rate $8 \times 10^{-16} m^3s^{-1}$ and absorption coefficient $255.8 m^{-1}$.

The best fit is estimated for the triplet $K_1=1.5 \times 10^{-19} m^3s^{-1}$, $K_r=1 \times 10^{-19} m^3s^{-1}$ and absorption coefficient $24,307 m^{-1}$. The ablation curve can be fitted by an exponential function with adjusted R-squared 0.9935 as: $Ab=17.91 \exp(0.002276Fl)-1049 \exp(-0.03186Fl)$, where Ab the ablation rate and Fl is the fluence all values in MKS units.

3.2 Parameters for 213 nm ablation

To find the best fit with the experimental results we calculated the least square errors and find the best combination of parameters. Table 4 shows only 4 combinations and Fig. 7 show the experimental results (small circles) according to Dair et. al. [32] and the calculated Ablation

rate versus fluence. Table 5 shows some of the parameters used to find the best fit.

The best fit parameters are $K_1=6 \times 10^{-20} m^3s^{-1}$, $K_r=1 \times 10^{-19} m^3s^{-1}$ and absorption coefficient $=17,015 m^{-1}$. The ablation curve can be fitted by an exponential function with an adjusted R-squared 0.9981 as: $Ab=17.91 \exp(0.002276 \times Fl) -1049 \exp(-0.03186 \times Fl)$, where Ab the ablation rate and Fl is the fluence all values in MKS units.

3.3 Parameters for 266 nm ablation

Using the ablation rate data measured by Soderberg et. al. [33]. Figure 8 illustrates some of the triplets in Table 6 in the case of 266 nm ablation. The following table summarizes the triplet parameters for each case. As the photon energy is lower than the 193 nm photon, the photonic flux is higher but the probability of photochemical reaction is lower. This explains the higher ablation threshold. From the experimental curve the rate of ablation is $6.3 \times 10^{-3} [um/(m)/cm^2]$: $Ab=-2.8 \times 10^7 F1^2+0.01084 \times FL -47.8$, where Ab the ablation rate and Fl is the fluence all values in MKS units.

3.4 Thermal effect during UV laser ablation

The maximum temperature depends on the wavelength, fluence and no of pulses. Figure 9 (a), (b), and (c) show the dependence of maximum temperature versus fluence for 50 pulses at 193 nm, 213 nm and 266 nm respectively.

Using the 193 nm laser, the temperature dependence on fluence can be fitted as: $T=0.1368 F1+296.789$. While at 213 nm and 266 nm, the temperature is approximately linearly dependent on laser fluence in this fluence range, where $T=0.1094 FL+297$, for 213 nm and $T=516.3+0.0625 FL$ for 266 nm. Table 7 summarizes the parameters of different laser corneal interaction showing the fluence to obtain 25 um ablation depth and the corresponding maximum temperature.

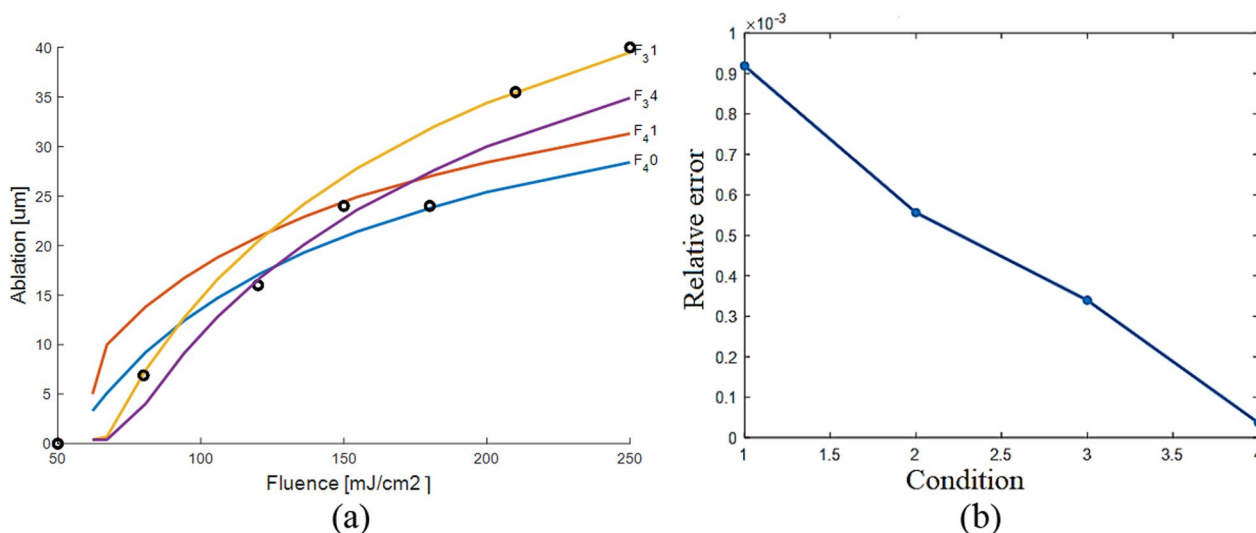


Fig. 7 **a** Ablation rate versus fluence for different combinations of reaction rates using 213 nm laser **b** the least square error

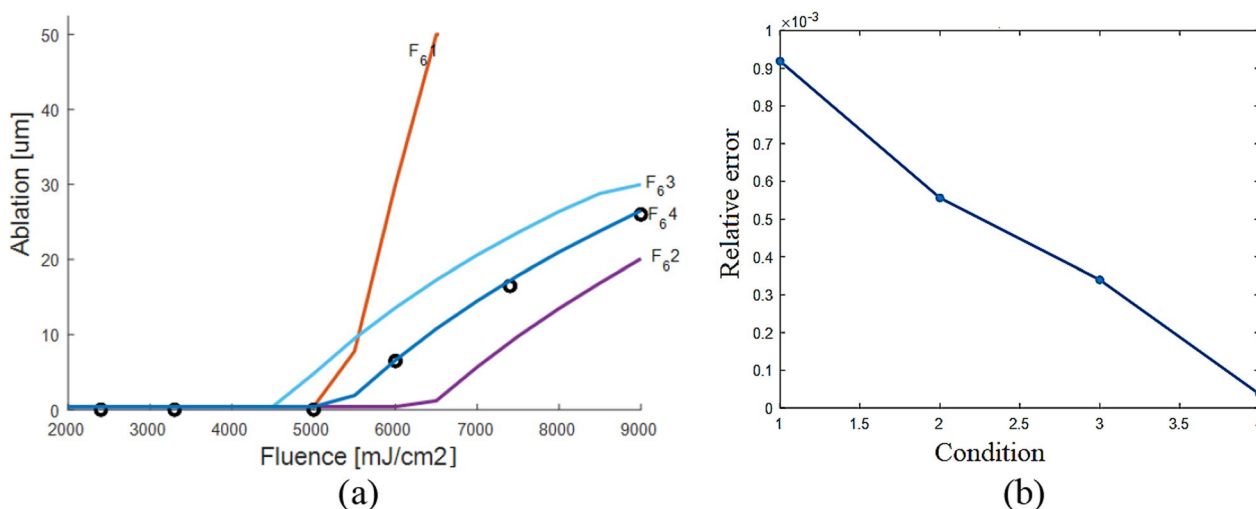


Fig. 8 **a** Ablation rate versus fluence for different combinations of reaction rates at 266 nm, **b** the least square error

Table 6 Parameters for 266 nm

	$K_1 \times 10^{-22}$ $m^3 s^{-1}$	$K_r \times 10^{-19}$ $m^3 s^{-1}$	Thermal absorption $[m^{-1}]$	Least square error $\times 10^{-4}$
F61	6	1	2180	9.19
F62	5	1	9723	5.5
F63	7	1	11,667	3.39
F64	6	1	10,930	0.36

The low ablation efficiency of the 266-nm system would require the use of high fluence that is not reasonable for clinical work. On the other hand the use of solid state 213 nm produced as 5th harmonic of YAG lasers is much better than the 193-nm excimer.

3.5 Threshold analysis

To study in more detail the parameters affect the startup of ablation. For 193 nm laser at 10 Hz repetition rate, we kept constant the fluence at 1000 mJ/cm² and varied the pulse duration. For pulse duration shorter than 1 ns, the start of ablation occurs at the third pulse. Then it starts to increase as the pulse duration increases. Where for fluence 100 mJ/cm² ablation starts at the 23rd pulsed until 1 ns pulses then it starts to increase. Reducing the fluence to 10 mJ/cm² delayed the ablation to the pulse number 221st until pulse duration 10 picosecond then it increases with increasing pulse duration.

For each Intensity, the interplay of the photochemical reaction and the reverse reaction leads to inhibition

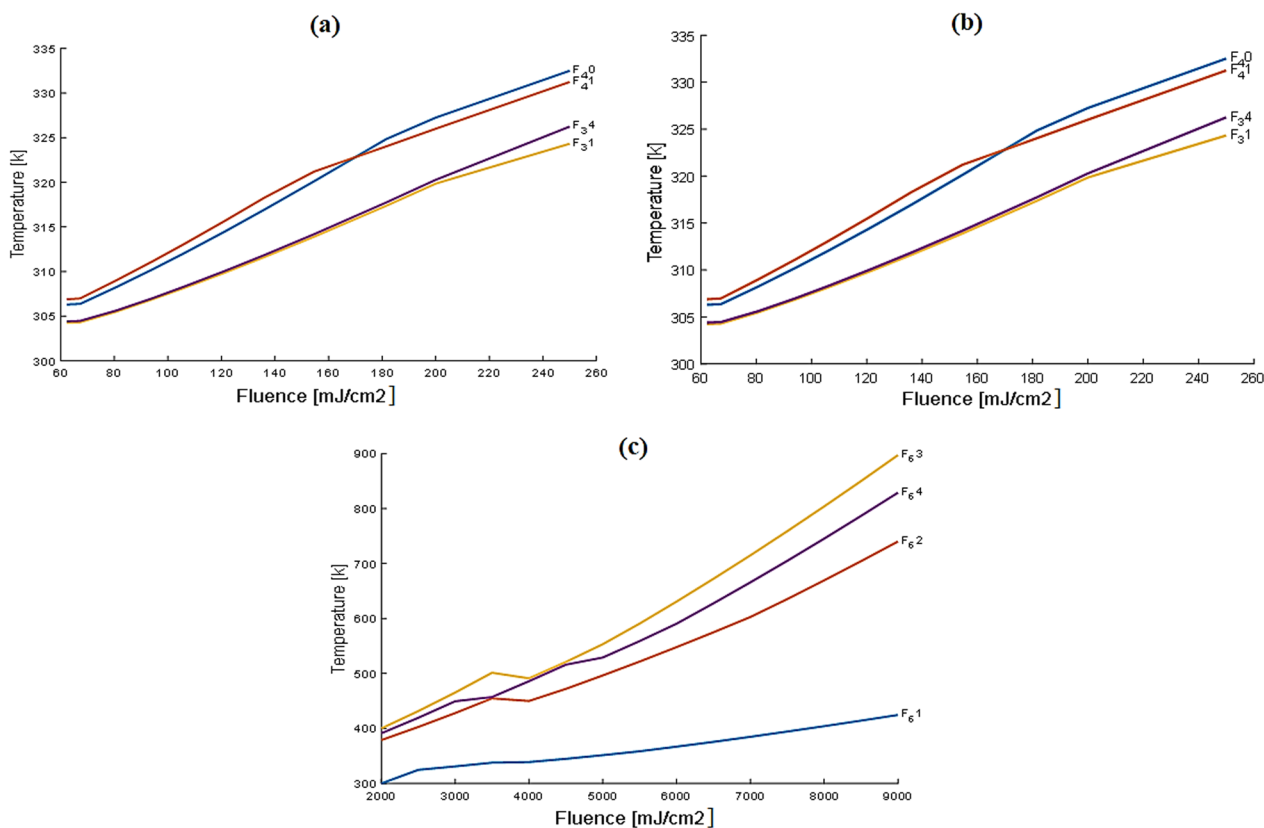


Fig. 9 Temperature versus fluence after 50 pulses using a 193 nm laser, b 213 nm laser, c 266 nm laser

Table 7 Parameters of different laser corneal interaction the corresponding maximum temperature

λ [nm]	K_1 [m^3s^{-1}]	a [m^{-1}]	Fluence [$mJcm^{-2}$]	Spot size (mm)	Pulse width (ns)	Max Temp. [k]
193	1×10^{-19}	24,307	180	0.7	4–7	324.4 (51.4 °C)
213	6×10^{-20}	17,015	182	0.6	10–12	317.5 (44.5 °C)
266	6×10^{-22}	10,938	9000	0.7	3–5	800.2 (527.2 °C)

of ablation until the accumulation of fragments dominates. We start to realize the ablation after (N) pulses depending on the fluence (F [Jm^{-2}]) as demonstrated in Fig. 10 according to the empirical relation: $F \times N^{0.891} = 1.521 \times 10^4 J/m^2$.

3.6 Predictions for UV ultrashort pulses with fluence

Considering a picosecond mode locked laser at 213 nm. The model predicts its behavior as follows. For a fluence $10 mJcm^{-2}$, pulse duration 10 picoseconds and repetition rate 10 kHz the ablation starts after 313 pulses with

ablation rate of $0.084 \mu m/pulse$. Increasing the fluence to $100 mJ cm^{-2}$ the ablation starts at pulse #32 with ablation rate of $0.46 \mu m/pulse$ the temperature rise to achieve $40 \mu m$ ablation is $324.6 K (51.6 °C)$ as shown in Fig. 11.

We studied some possible effects of a femtosecond laser with Fluence= $10 Mj cm^{-2}$; pulse duration 10 fs and repetition rate 10 kHz. Ablation starts after 0.034 s i.e. after 340 pulses. The temperature is $308.5 K (35.5 °C)$ for $100 mJ cm^{-2}$ ablation starts after the 32 pulse with ablation rate $0.407 \mu m/pulse$ and temperature $324 K (51.5 °C)$.

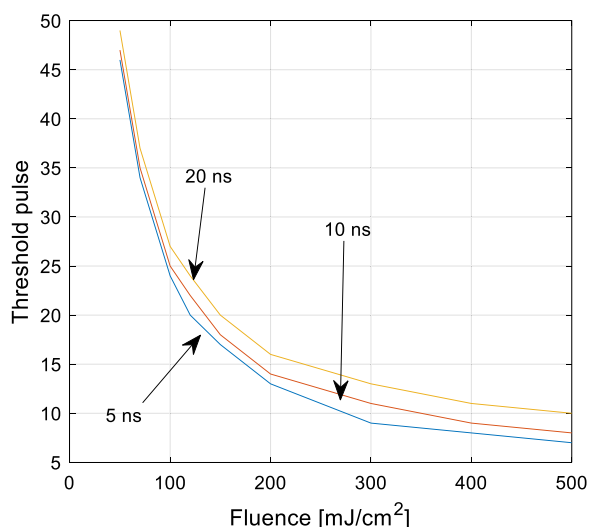


Fig. 10 Ablation starts at pulse N for different Fluence

4 Discussion

In our calculations, we distinguish between absorption coefficient which describes the total absorption including energy absorbed during photochemical reaction and energy converted to heat (thermal absorption part). The latter one is small fraction of the first. When using low

light fluence the temperature rise is relatively small. We didn't take into consideration the cooling which is clearly very important as our calculations showed. However, we considered a system where the spot is fixed; this is not the case of practical systems which use flying spots that reduce very much the temperature in addition to cooling the eye. Additionally, the proposed model used a Gaussian beam but a 15- μm mask is placed in front of the cornea. Therefore the shape in results may sometimes appear similar to the top hat pulses (see Fig. 5(F) and (H)).

The measured values of the absorption coefficient in the literature are mostly due to the absorbed photons during the photochemical reaction, the contributed portion to thermal effect is smaller than this measured values. The onset of ablation is the balance between the rate of bond dissociation and recombination processes. We estimated these rates in our proposed model for the wavelengths 193 nm, 213 and 266 nm. These rates also have an effect on the temperature rise during ablation. The use of femtosecond laser pulses at the UV is predicted to have a negligible temperature rise.

In order to verify our model we used the data given by Krueger et. al. [34]. They stated that threshold for several pulse repetition rates and laser wavelength are not constant. We present a part of their data in the Table 8.

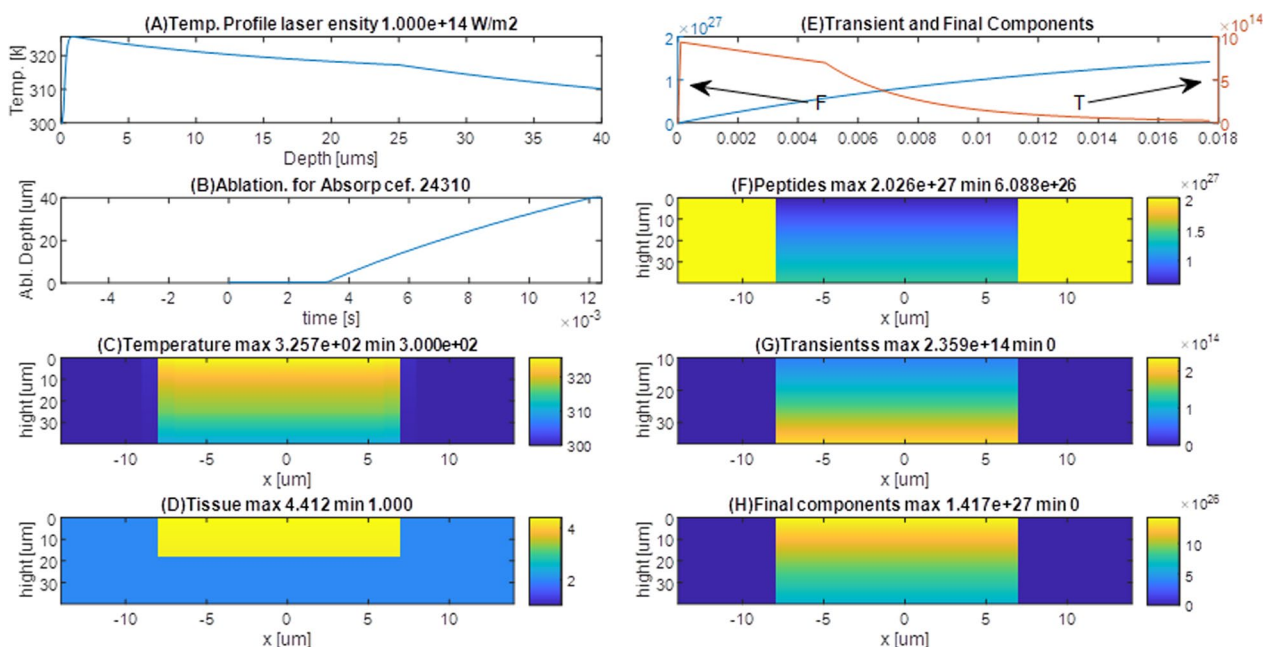


Fig. 11 Expected results of femtosecond laser ablation, **A** the temperature profile after 50 pulses along the laser axis, **B** the variation in the thermal absorption coefficient with time, **C** the spatial distribution of temperature, **D** at corneal tissue **E** Transient and final components, **E** transient and final components, **F** peptide molecules density, **G** transient products density, **H** final components

Table 8 The threshold values

Laser wavelength	Pulse repetition rate		
	1 Hz	10 Hz	25 Hz
193 nm	50 ± 13	50 ± 10	55 ± 10
249 nm	185 ± 20	120 ± 20	80 ± 25
308 nm	540 ± 80	500 ± 50	420 ± 40

For laser at 193 nm the error in the threshold makes it difficult to find the trend. However for 249 nm and 308 nm it is clear that the threshold decreases with increasing the pulse rate. This means that when decreasing the fluence ablation starts after more pulses and so for a fixed exposure time we need higher pulse rate.

It is crucial to recognize that the suggested model might not fully capture the complexities and biological processes involved in corneal photochemical reactions since mathematical models are frequently simplifications of complicated biological systems. This constraint results from the model's assumptions and simplifications. Additionally, mathematical models rely on input parameters, such as reaction rates, cross-sections, and absorption coefficients. These parameters may have inherent uncertainty or may be obtained from experimental studies with their own limitations. As more experimental data becomes available, it would be beneficial to refine the parameters used in the mathematical model. By fitting the model to experimental results, you can improve the accuracy of the model's predictions and reduce the uncertainty associated with the input parameters. This parameter refinement process would contribute to the robustness of the methodology and its applicability to different measuring problems.

5 Conclusions

In the current study, we presented a model for corneal ablation using non-moving laser spot with three different laser wavelengths 193 nm, 213 nm and 266 nm. The model didn't attempt to calculate the temperature rise when using flying spot systems but it aimed to compare these systems under the same conditions. Moreover, the model introduces the concept of reverse chemical reaction which makes clear the very well observed phenomena of ablation threshold. An absolute requirement is that the ablation per pulse is small enough to allow high precision ablation (<0.5 μm) but large enough to make the total ablation time reasonable. The laser ablation with wavelength 266 nm results in an elevated temperature of the tissues. This may lead in turn to thermal damage of the tissues. So our recommendation is to use 213 nm solid state nanosecond and femtosecond lasers. The temperature in the three cases is nearly linearly dependent on the fluence of the laser.

Currently, our study is just to compare the effect of different wavelengths on the ablation model. Introducing cooling and flying spot techniques will be the next step in the model. Moreover, the suggested methodology would benefit greatly from experimental research validating the results of the mathematical model. The cornea's photochemical reactions and ablation thresholds can be measured in vitro or in vivo, which could yield useful information for model validation. The model's dependability and accuracy would increase as a result, and its applicability to other measurement issues would be strengthened. Furthermore, combining the mathematical model with imaging techniques, such as optical coherence tomography (OCT) or confocal microscopy, could provide real-time feedback during laser procedures. This integration would enable the model to account for variations in corneal geometry and monitor the progress of the photochemical reactions. By incorporating imaging techniques, the methodology could be extended to address measuring problems that require precise monitoring and control. While this manuscript focuses on corneal reshaping, the methodology could be adapted and applied to other tissues or materials. Considering the specific properties and photochemical reactions of different tissues would allow the methodology to be utilized in a broader range of measuring problems beyond corneal reshaping.

Acknowledgements

Not applicable

Author contributions

SH and IA conceived and designed the study; OH, SA, and AH conducted the analyses and contributed to the data collection; SH, OH and IA drafted the manuscript. All authors read and approved the final manuscript.

Funding

Not applicable.

Availability of data and materials

All necessary data analyzed during this study are included in this published article. Any additional data could be available from the corresponding author upon request.

Declarations

Ethics approval and consent to participate

Not applicable.

Consent for publication

Not applicable.

Competing interests

The authors have no relevant financial or non-financial interests to disclose.

Received: 29 August 2023 Accepted: 24 September 2023

Published online: 06 November 2023

References

- Maayah B, Arqub OA (2023) Hilbert approximate solutions and fractional geometric behaviors of a dynamical fractional model of social media addiction affirmed by the fractional Caputo differential operator. *Chaos, Solitons Fract X* 10:100092. <https://doi.org/10.1016/j.csfx.2023.100092>
- Arqub OA, Maayah B (2023) Adaptive the Dirichlet model of mobile/immobile advection/dispersion in a time-fractional sense with the reproducing kernel computational approach: formulations and approximations. *Int J Mod Phys B* 37:2350179. <https://doi.org/10.1142/S0217979223501795>
- Maayah B, Moussaoui A, Bushnaq S, Abu Arqub O (2022) The multistep Laplace optimized decomposition method for solving fractional-order coronavirus disease model (COVID-19) via the Caputo fractional approach. *Demonstratio Math* 55:963–977. <https://doi.org/10.1515/dema-2022-0183>
- Maayah B, Abu Arqub O, Alnabulsi S, Alsulami H (2022) Numerical solutions and geometric attractors of a fractional model of the cancer-immune based on the Atangana-Baleanu-Caputo derivative and the reproducing kernel scheme. *Chin J Phys* 80:463–483. <https://doi.org/10.1016/j.cjph.2022.10.002>
- Kugler LJ, Wang MX (2010) Lasers in refractive surgery: history, present, and future. *Appl Opt* 49:1–9. <https://doi.org/10.1364/AO.49.0000F1>
- Raman Y (2015) Refractive and visual outcomes of laser in situ keratomileusis for moderate to high myopia using 213nm solid state laser - a four year follow up study. *Delhi J Ophthalmol* 26:25–29. <https://doi.org/10.7869/djo.130>
- Pidro A, Biscevic A, Pjano MA et al (2019) Excimer lasers in refractive surgery. *Acta Inform Med* 27:278–283. <https://doi.org/10.5455/aim.2019.27.278-283>
- Motta S, Pappalardo F (2013) Mathematical modeling of biological systems. *Brief Bioinform* 14:411–422. <https://doi.org/10.1093/bib/bbs061>
- Ravi L, Sreenivas BKA, Kumari GRS, Archana O (2022) Anticancer cytotoxicity and antifungal abilities of green - synthesized cobalt hydroxide (Co(OH)₂) nanoparticles using *Lantana camara* L. *Beni-Suef Univ J Basic Appl Sci* 11:1–14. <https://doi.org/10.1186/s43088-022-00304-1>
- Tarabichi S, Al-Raei M, Solieva O (2022) Improving the accuracy of tumor surgery by THz imaging and making the results of pathological anatomy faster by THz spectroscopy. *Beni-Suef Univ J Basic Appl Sci* 11:51–54. <https://doi.org/10.1186/s43088-022-00201-7>
- Taflove A, Brodwin ME (1975) Computation of the electromagnetic fields and induced temperatures within a model of the microwave-irradiated human eye. *IEEE Trans Microw Theory Tech* 23:888–896. <https://doi.org/10.1109/TMTT.1975.1128708>
- Al-Badwaih KA, Youssef AB (1977) Biological thermal effect of microwave radiation on human eyes. *Biol Effects Electromag Waves* 1:61–78
- Scott JA (1988) A finite element model of heat transport in the human eye. *Phys Med Biol* 33:227–242. <https://doi.org/10.1088/0031-9155/33/2/003>
- Lagendijk JJW (1982) A mathematical model to calculate temperature distributions in human and rabbit eyes during hyperthermic treatment. *Phys Med Biol* 27:1301–1311. <https://doi.org/10.1088/0031-9155/27/11/001>
- Zhou Z, Sun W, Wu J et al (2023) The fundamental mechanisms of laser cleaning technology and its typical applications in industry. *Processes* 11:1–17. <https://doi.org/10.3390/pr11051445>
- Abdelhalim I, Hamdy O, Hassan AA, Elnaby SH (2021) Assessing the local temperature of human cornea exposed to surface ablation by different laser refractive-surgery devices: a numerical comparative study. *Lasers Med Sci* 36:1725–1731. <https://doi.org/10.1007/s10103-021-03347-5>
- Pettit GH, Sauerbrey R (1993) Pulsed ultraviolet laser ablation. *Appl Phys Solid Surf* 56:51–63. <https://doi.org/10.1007/BF00351903>
- Fisher BT, Hahn DW (2007) Development and numerical solution of a mechanistic model for corneal tissue ablation with the 193 nm argon fluoride excimer laser. *J Opt Soc Am A* 24:265. <https://doi.org/10.1364/josaa.24.000265>
- Tokarev VN, Lunney JG, Marine W, Sents M (1995) Analytical thermal model of ultraviolet laser ablation with single-photon absorption in the plume. *J Appl Phys* 78:1241–1246. <https://doi.org/10.1063/1.360365>
- Sutcliffe E, Srinivasan R (1986) Dynamics of UV laser ablation of organic polymer surfaces. *J Appl Phys* 60:3315–3322. <https://doi.org/10.1063/1.337698>
- Srinivasan R, Braren B, Seeger DE, Dreyfus RW (1986) Photochemical cleavage of a polymeric solid: details of the ultraviolet laser ablation of poly(methyl methacrylate) at 193 and 248 nm. *Macromolecules* 921:916–921
- Eldin H, Ahmad M, Abd K et al (2022) Pentacam versus anterior segment OCT in measuring intended versus achieved ablation depth post - myopic LASIK correction. *Beni-Suef Univ J Basic Appl Sci* 11:1–7. <https://doi.org/10.1186/s43088-022-00235-x>
- Snell RS, Lemp MA (2013) *clinical-anatomy of-the-eye*. Wiley
- Mirnezami SA, Jafarabadi MR, Abrishami M (2013) Temperature distribution simulation of the human eye exposed to laser radiation. *Laser Med Sci* 4:175–181
- Abdelhalim I, Hamdy O, Ahmed A et al (2021) Dependence of the heating effect on tissue absorption coefficient during corneal reshaping using different UV lasers : a numerical study. *Phys Eng Sci Med* 44:221–227. <https://doi.org/10.1007/s13246-021-00971-x>
- Kolozsvári L, Nógrádi A, Hopp B, Bor Z (2002) UV absorbance of the human cornea in the 240- to 400-nm range. *Invest Ophthalmol Vis Sci* 43:2165–2168
- LaserSoft – UV ablation laser, <http://katalanaser.com/products/lasersoft/> A 5 M 2020 LaserSoft – UV ablation laser, <http://katalanaser.com/products/lasersoft/>, Accessed 5 May 2020. <http://katalanaser.com/products/lasersoft/>. Accessed 5 May 2020
- Vaghiasya H, Krause S, Miclea P-T, Authors AIF, other works by these, (2023) Fundamental study of a femtosecond laser ablation mechanism in gold and the impact of the GHz repetition rate and number of pulses on ablation volume. *Opt Mater Express* 13:982–996. <https://doi.org/10.1364/OME.474452>
- Abdelhalim I, Hamdy O, Khattab MA et al (2023) Evaluating the efficacy of Nd:YAG fourth harmonic (266 nm) in comparison with ArF excimer (193 nm) in laser corneal reshaping: ex vivo pilot study. *Int Ophthalmol* 43:3087–3096. <https://doi.org/10.1007/s10792-023-02708-z>
- Abdelhalim I, Hamdy O, Hassan AA, Elnaby SH (2021) Nd: YAG fourth harmonic (266-nm) generation for corneal reshaping procedure: an ex-vivo experimental study. *PLoS ONE* 16(11):e0260494. <https://doi.org/10.1371/journal.pone.0260494>
- Munnerlyn CR, Arnoldussen ME, Munnerlyn AL, Logan BA (2006) Theory concerning the ablation of corneal tissue with large-area, 193-nm excimer laser beams. *J Biomed Opt* 11:064032. <https://doi.org/10.1117/1.2399091>
- Dair GT, Pelouch WS, Van Saarloos PP et al (1999) Investigation of corneal ablation efficiency using ultraviolet 213-nm solid state laser pulses. *Invest Ophthalmol Vis Sci* 40:2752–2756
- Soderberg PG, Manns F, Sulhorn S et al (2003) Corneal ablation rate at 266 nm. *Proc SPIE* 4951:77–82. <https://doi.org/10.1117/12.482465>
- Krueger RR, Trokel SL, Schubert HD (1985) Interaction of ultraviolet laser light with the cornea. *Invest Ophthalmol Vis Sci* 26:1455–1464

Publisher's Note

Springer Nature remains neutral with regard to jurisdictional claims in published maps and institutional affiliations.

Submit your manuscript to a SpringerOpen® journal and benefit from:

- Convenient online submission
- Rigorous peer review
- Open access: articles freely available online
- High visibility within the field
- Retaining the copyright to your article

Submit your next manuscript at ► [springeropen.com](https://www.springeropen.com)